

Supplementary Information

Near-field digital holography: a tool for plasmon phase imaging

P. Dvořák^{1,2,*}, M. Kvapil^{1,2}, P. Bouchal^{1,2}, Z. Édes^{1,2}, T. Šamořil^{1,2}, M. Hrtoň^{1,2}, F. Ligmajer^{1,2}, V. Křápek^{1,2}, and T. Šikola^{1,2}

¹ Central European Institute of Technology, Brno University of Technology, Purkyňova 123, 612 00 Brno, Czech Republic

² Institute of Physical Engineering, Brno University of Technology, Technická 2, 616 69 Brno, Czech Republic

1. Plasmon interference for a circular slit

A single nano-aperture drilled into a gold film serves under linearly polarized illumination as a point source for plasmon waves. Sufficiently far away from the aperture, the out-of-plane electric field component of the plasmon wave at the air-gold interface assumes the following form¹

$$E_z(\rho, \varphi) = AH_1^{(1)}(\rho k_{\text{SPP}}) \cos(\varphi).$$

Here, the cylindrical coordinates ρ and φ describe the position with respect to the aperture, k_{SPP} is the in-plane wave vector of freely propagating SPPs on the gold film, A is the amplitude of the wave and $H_1^{(1)}(x)$ stands for the Hankel function of the first kind. The wave incident on the aperture is assumed to be polarized along the x -axis. For distances larger than several plasmon wavelengths, the Hankel function can be approximated by its asymptotic form so that

$$E_z(\rho, \varphi) \approx A \sqrt{\frac{2}{\pi \rho k_{\text{SPP}}}} \exp(i\rho k_{\text{SPP}}) \exp\left(-i\frac{3}{4}\pi\right) \cos \varphi.$$

Now let us consider a circular slit of radius R illuminated with an x -polarized plane wave (normal incidence). Similarly to the nano-aperture, the individual sections of the circular slit will also be a source of SPPs, except we need to take into account the fact that the amplitude of the excited plasmons will locally depend on the mutual orientation of the slit and the polarization direction of the incident wave.² Consequently, the contribution to the out-of-plane electric field from a small section of the circular slit can be expressed as

$$dE_z(r, \varphi) = d\varphi' \frac{A}{2\pi} \sqrt{\frac{2}{\pi k_{\text{SPP}} |\mathbf{r} - \mathbf{r}'|}} \exp(ik_{\text{SPP}} |\mathbf{r} - \mathbf{r}'|) \exp\left(-i\frac{3}{4}\pi\right) (\hat{\mathbf{x}} \cdot \mathbf{n}) [\mathbf{n} \cdot (\mathbf{r} - \mathbf{r}')],$$

Where $\mathbf{r} = (r \cos \varphi, r \sin \varphi, 0)$ is the position at which the field is calculated and $\mathbf{r}' = (R \cos \varphi', R \sin \varphi', 0)$ is the position vector of the source. Let us focus now only at the central part of the area surrounded by the circular slit so that the condition $R \gg r$ is satisfied. The above expression can be then approximated by

$$dE_z(r, \varphi) \approx -d\varphi' \frac{A}{2\pi} \sqrt{\frac{2}{\pi k_{\text{SPP}}}} \frac{\exp(ik_{\text{SPP}} R)}{\sqrt{R}} \exp\left(-i\frac{3}{4}\pi\right) \exp[-ik_{\text{SPP}} r \cos(\varphi' - \varphi)] \cos \varphi'.$$

Finally, the total field is obtained by integration over φ'

$$E_z(r, \varphi) \approx iA \sqrt{\frac{2}{\pi k_{\text{SPP}}}} \frac{\exp(ik_{\text{SPP}}R)}{\sqrt{R}} \exp\left(-i\frac{3}{4}\pi\right) J_1(k_{\text{SPP}}r) \cos \varphi. \quad (1)$$

Fig. S1 compares the above analytical result with the fully numerical FDTD calculations and reveals only minor differences between those two. Usually, the distance between two neighboring interference maxima gives us directly the plasmon wavelength (or more precisely its half), but that does not generally hold for plasmon waves with curved wavefront, which is incidentally our case. As we have already shown, the interference pattern produced by the circular slit is described by an oscillating Bessel function $J_1(k_{\text{SPP}}r)$. For sufficiently large arguments, its period of oscillations is indeed λ_{SPP} , but close to the origin it is not so. Therefore, when we estimate the plasmon wavelength from the distance between two interference maxima, the inclusion of those close to the center of our interference pattern will inevitably shift our estimate towards higher values, exceeding even the free space wavelength. This effect can be clearly seen in Fig. S2, where we plot the spatial period of interference maxima as a function of the number of maxima N that are taken into account. We start with the two innermost maxima ($N = 2$) and then gradually spread outwards, with each step adding the two closest maxima on the left and right hand side. Apparently, if we take only few maxima from the central part of the field profile, our estimate of λ_{SPP} will be significantly larger than the wavelength of the freely propagating plasmon with a straight wavefront. The situation somewhat improves as we include more distant maxima, but the only viable solution seems to be to exclude the "problematic" central maxima (see green crosses in Fig. S2) or to completely abandon the idea of extracting the plasmon wavelength from this type of interference pattern.

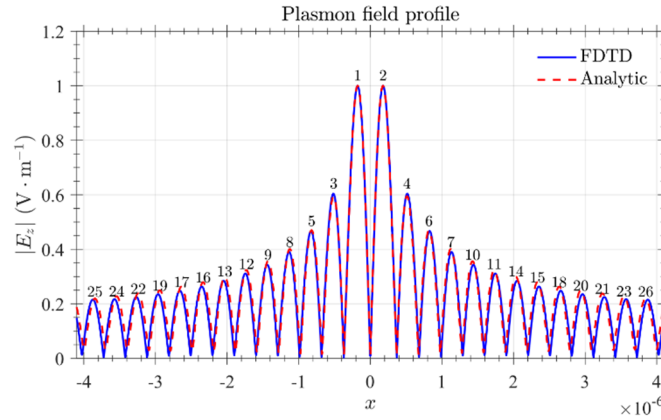


Fig. S1: The calculated field profile along the horizontal axis of mirror symmetry. The profile calculated analytically from eq 1 (red dashed line) deviates only slightly from the profile obtained by the FDTD calculations (blue solid line). The numbers above individual maxima indicate their ordering.

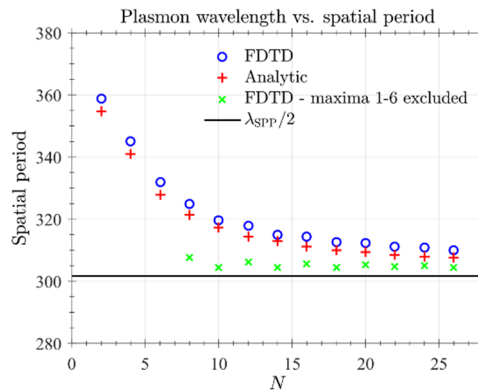
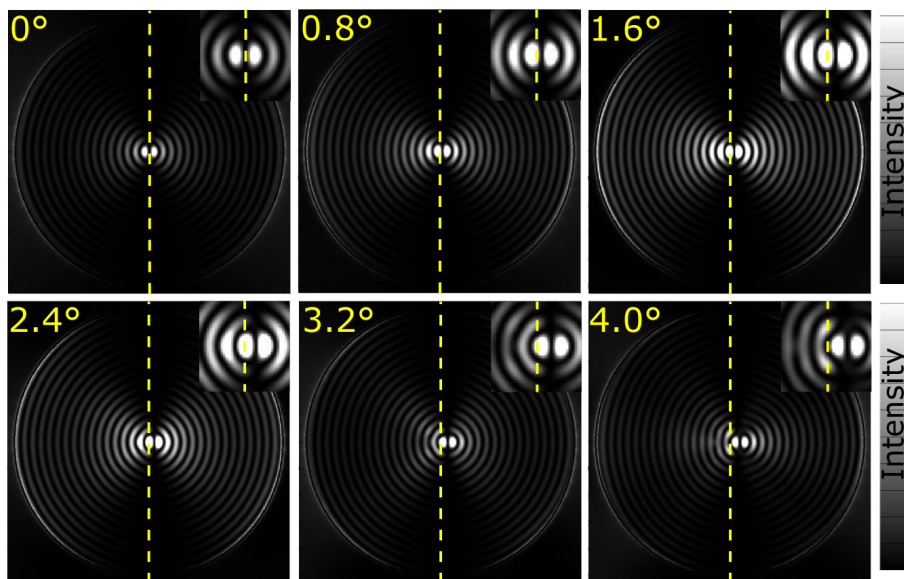


Fig. S2: The spatial periods of the electric field maxima shown in Fig. S1 as a function of the number of maxima N that are taken into account. The order in which the maxima are taken is indicated by numbers in Fig. S1, i.e. we start with the two innermost ones and gradually spread outwards. The blue circles and red pluses mark the spatial period estimates obtained from FDTD and analytic calculations, respectively. The green crosses correspond to estimates in which the 6 innermost maxima have been excluded. The black line marks the half-wavelength of a plasmon with a straight wavefront.

2. The tilt of sample

The phase shift between the two SPP waves can be experimentally achieved even without SLM just by tilting of the sample. In that case, the phase shift arises as a consequence of varying optical path of the excitation beam. For our circular slit and fused silica substrate, 4.2 degrees tilt of the sample results in the shift of the interference pattern by half of the SPP wavelength. The dependence between the sample tilt and the shift of interference patterns calculated by FDTD simulation is plotted in Fig. S3. Although it indicates a good compliance between phase shifts introduced by the SLM (see Fig. S4) and the tilt of the sample, tilting has an additional undesired effect on the interference pattern. Namely, the envelope function of the measured intensity profile loses its central symmetry and the position of maximum intensity shifts from the centre of the slit. This effect makes the controlling the phase of the SPP waves via a sample tilt inapplicable for our method of PPDH. However, the SLM could be used for the sample tilt correction in case of small angles up to 4.2 degrees.



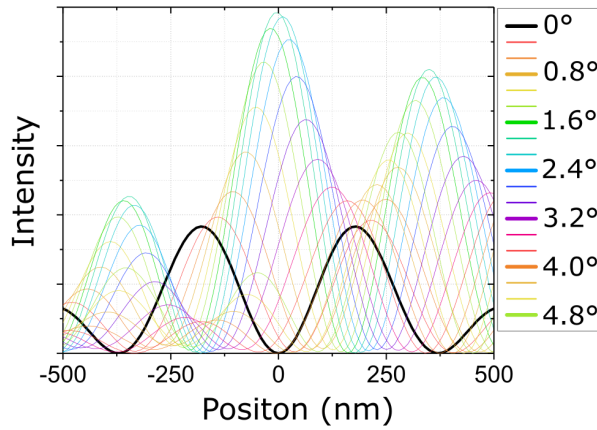


Fig. S3: Simulated interference patterns for the different tilting angles of the sample (the axis of vertical symmetry is highlighted with the white dotted line). The graph shows the normalized intensity profiles at the center along the horizontal axis of symmetry. Note, that the profile is asymmetric and the difference between the maximal intensities is also higher than in case of the phase-shifting.

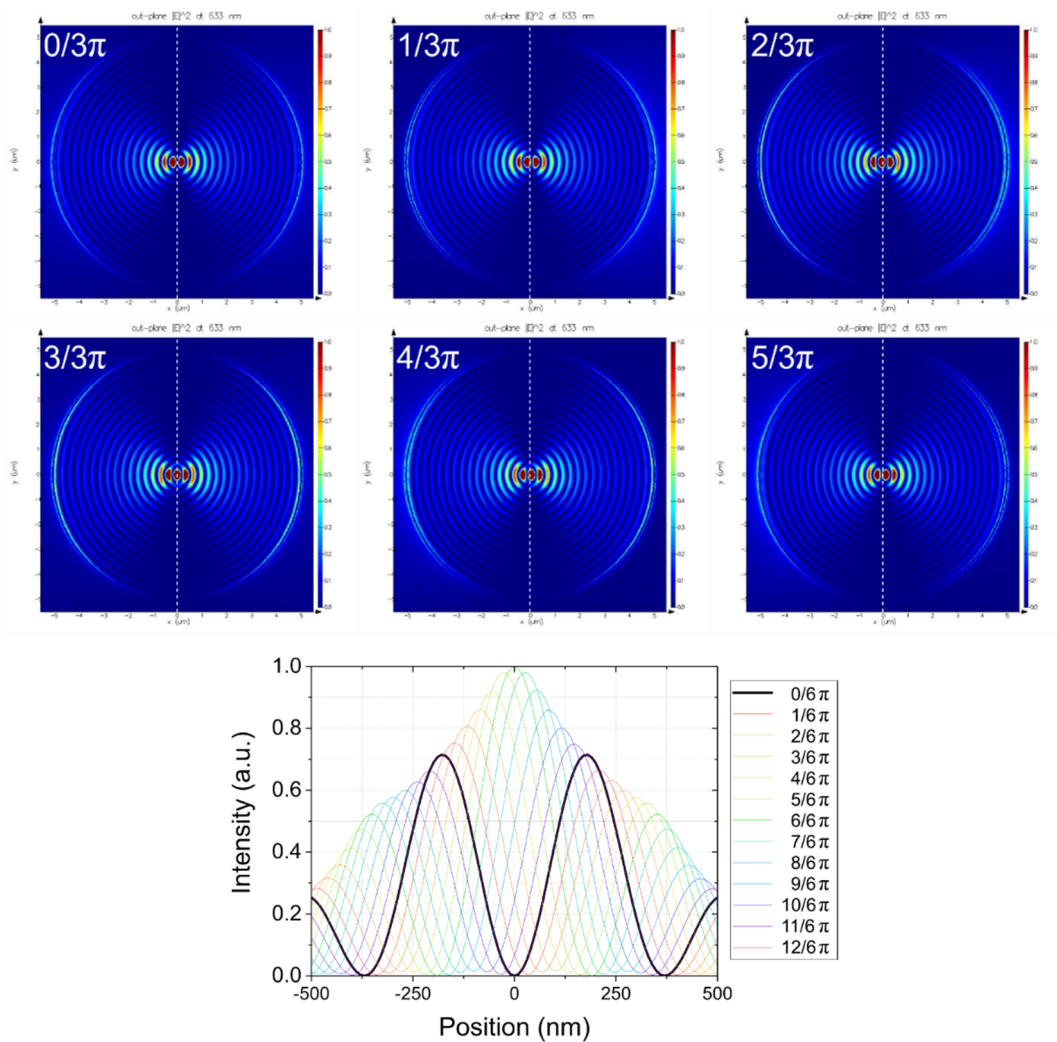


Fig. S4: Simulated interference patterns for different phase-shifts between the two half-circles (the axis of vertical symmetry is highlighted with the white dotted line). The graph shows the normalized intensity profiles along the horizontal axis of symmetry for different phase-shifts at the center.

Similarly to the case of two interfering plasmons, the interference pattern of a single propagating plasmon and the incident plane wave is sensitive to the tilt of the sample. Given the geometry of our sample, we can consider two independent tilting directions denoted by angles ξ and ζ . Here ξ describes the rotation of the sample about the symmetry axis of our V-structure (see the schematics in Fig. S8c), while ζ gives us the tilt in the direction of the propagation of the Cosine-Gauss beam (see the schematics in Fig. S8d). Generally, ξ and ζ can be non-zero simultaneously. We shall, however, investigate these two types of tilt separately, as they distort the interference pattern in a qualitatively different way and also to keep the expressions lucid. To further simplify things (without losing the important aspects of the interference patterns) we shall make the assumption that sufficiently far away from the slits the SPPs launched from the slits have approximately a straight wavefront. (That this is true is clear from the numerical simulations.) Without any tilt, the wavefront will be parallel to the slit. When a tilt is present, the phase of the incident light varies as we move along the slit and so does the phase of the excited plasmon wave. Based on simple geometrical considerations, the overall effect is that the SPP wavefront is no longer parallel to the slit but it is slightly skewed. The deflection angle γ between the original and the new SPP propagation direction naturally depends on the type and magnitude of the tilt. Apart from the propagation direction, the tilt can also affect the periodicity of the interference pattern. To provide some estimate of how large these two effects can be, we used a simplified representation of the interfering waves and analytically calculated the resulting interference pattern.

First, let us focus on the tilt about the symmetry axis of our V-structure denoted by ξ . Assuming ξ is small, the electric field intensity at the gold-air interface can be approximately written as

$$|\vec{E}|^2 \approx A_0^2 + 4A_{\text{SPP}}^2 \cos^2[k_{\text{SPP}} \sin \delta (x \sin \gamma - y \cos \gamma)] + 4A_0 A_{\text{SPP}} \cos[k_{\text{SPP}} \sin \delta (x \sin \gamma - y \cos \gamma)] \cos(k_{\text{SPP}} \cos \delta x),$$

where A_0 and A_{SPP} are the amplitudes of the transmitted plane wave and a single SPP wave, k_{SPP} is the propagation wavevector of the SPP, k_0 is the free space wavevector, δ stands for the inclination angle of our V-structure $\delta = 5^\circ$ for our structure, and the sine and cosine of the deflection angle γ are given by

$$\sin \gamma = \frac{k_0 \sin \xi}{k_{\text{SPP}}} \cos \delta, \quad (2)$$

$$\cos \gamma = \sqrt{1 - \left(\frac{k_0 \sin \xi}{k_{\text{SPP}}} \cos \delta \right)^2}.$$

The first two terms in the above approximate expression for the electric field intensity correspond to the pure transmitted and plasmon fields, while the third term gives us the interference pattern. Note that the interference fringes (given by $\cos(k_{\text{SPP}} \cos \delta x)$) remain parallel to the y -axis and the tilt manifests itself only in the change of the propagation direction of the whole Cosine-Gauss beam which is shifted by the deflection angle γ . This is apparent from the term $\cos[k_{\text{SPP}} \sin \delta (x \sin \gamma - y \cos \gamma)]$ which defines the cosine envelope of the beam. Choosing $\xi = 5^\circ$, we calculated the interference pattern using FDTD (see the field maps in Fig. S8c) and then compared the deflection angle γ of the Cosine-Gauss beam to the value

provided by the above simplified model. The value $\gamma \approx 4.77^\circ$ extracted from the numerical simulation was found to be very close to the prediction $\gamma = 4.81^\circ$. According to the model, changing the sign of ξ only flips the sign of the deflection angle γ while preserving its magnitude. The resulting interference pattern should be, therefore, only the mirror image of the other. This was also corroborated by our FDTD simulations (see Fig. S8c).

Next, we shall turn our attention towards the effects of the tilt in the direction of the Cosine-Gauss beam propagation labeled as ζ . Using the same assumptions as before, we can again construct an approximate expression for the electric field intensity at the gold-air interface

$$|\vec{E}|^2 \approx A_0^2 + 4A_{\text{SPP}}^2 \cos^2[k_{\text{SPP}} \sin \delta y] + 4A_0 A_{\text{SPP}} \cos[k_{\text{SPP}} \sin \delta y] \cos[(k_{\text{SPP}} \cos \delta x - k_0 \sin \zeta)x].$$

Note that since both δ and ζ are small, the phase variation along the slit is marginal and so is the deflection angle γ and we can therefore neglect it altogether in our analysis. Importantly, the tilting angle ζ appears only in the last term, where it affects the periodicity of the interference fringes: the tilt can cause the fringes to spread apart or squeeze together, depending on the sign of ζ (see the field maps in Fig. S8d). The new fringe periodicity $\Lambda(\zeta)$ can be easily calculated as

$$\Lambda(\zeta) = \frac{\lambda_0}{\frac{\lambda_0}{\lambda_{\text{SPP}}} \cos \delta - \sin \zeta}, \quad (3)$$

where λ_0 and λ_{SPP} are the free space and SPP wavelengths, respectively. To verify our simplified model, we compared it once again to the results of FDTD simulations. Fig. S8e shows the intensity profile along the main axis of the Cosine-Gauss beam calculated by FDTD for several values of the tilting angle ζ . From these, we determined the fringe periodicity and plotted it together with the above analytical expression in Fig. S8f. The agreement between the analytical model and the FDTD calculations is almost perfect.

The presented model not only helps us to understand how the tilt affects the interference pattern, it also enables us to estimate the actual sample tilt in the experiment. Fig. S8a shows the measured SNOM image of the Cosine-Gauss beam that interferes with the transmitted part of the illuminating plane wave. Apparently, the Cosine-Gauss beam is skewed with respect to the mirror symmetry axis of the V-structure which is an indication of a non-zero ξ -tilt. We estimated the deflection angle of the beam to be roughly $\gamma = 7.6^\circ$ which, according to Eq. (2), corresponds to a tilt of approximately $\xi \approx 8^\circ$. Next, we took a look at the periodicity of the experimentally observed interference fringes. Fig. S8b contains an intensity profile along the dashed white line drawn in Fig. S8a. The fringe periodicity was determined to be $\Lambda(\zeta) = 640$ nm which gives us after insertion into Eq. (3) a tilt of $\zeta \approx 3^\circ$. We should note that the estimation of the tilt derived from the beam deflection is much more unreliable than its periodicity-derived counterpart. This is due to the problematic recognition of the main axis of the Cosine-Gauss beam in the experiment. On the other hand, the interference fringes are very well resolved and their periodicity can be determined with a good accuracy. Furthermore, the fringe periodicity is also quite sensitive to the magnitude of the tilt (see Fig. S8f). This makes this kind of a setup a practical indicator of the tilt in SNOM measurements, especially

in those where we need to know the tilt with a good precision or need to get rid of it. In this respect, one can think of two isolated, mutually perpendicular slits that would serve as calibrated gauges of the tilt in the two possible tilting directions.

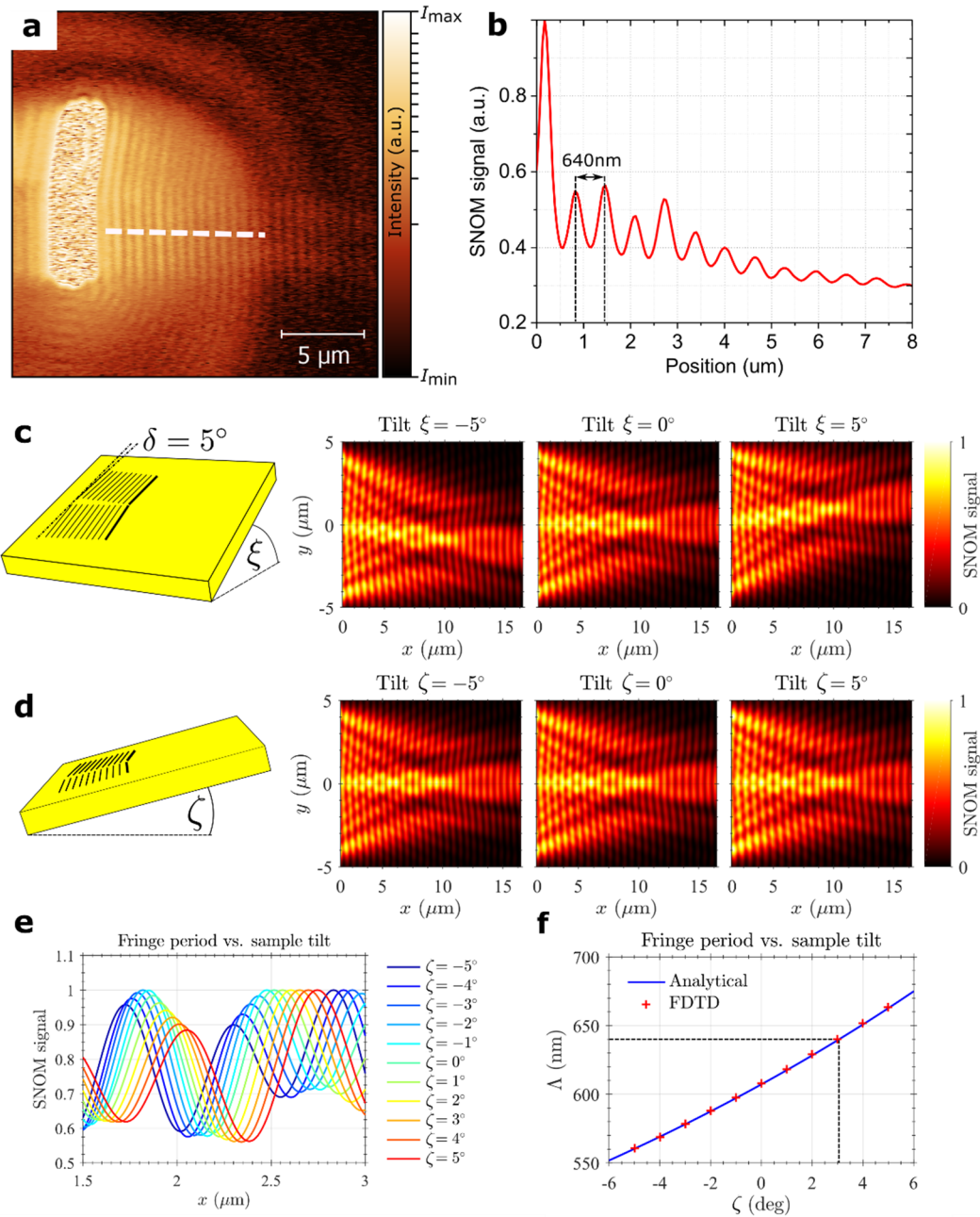


Fig. S5: **a** Experimental SNOM image of the Cosine-Gauss beam interfering with the transmitted portion of the incident plane wave. The white dashed line indicates the line along which the intensity profile plotted in **b** was taken. **c** Graphic representation of the tilt corresponding to the rotation of the sample around the symmetry axis of our V-structure and its impact on the interference pattern for various values of the angle ξ . **d** Graphic representation of the tilt along the propagation direction of the Cosine-Gauss beam and its impact on the interference pattern for various values of the angle ζ . **e** Intensity profiles along the main axis of the Cosine-Gauss beam calculated by FDTD for various values of the tilting angle ζ . **f** Fringe periodicity as a function of the tilting angle ζ . The blue line comes from the

simplified analytical model, while the points marked by red pluses were obtained from the FDTD calculated intensity profiles shown in e. The dashed black line indicates the ζ -tilt in our experimental setup that was estimated based on the fringe periodicity of the intensity profile plotted in b.

3. The experimental noise

In case of the phase reconstructed from the simulations without introducing noise (Fig. 3(b)) the phase changes linearly precisely from $-\pi$ to $+\pi$ and it flips at one point back from $+\pi$ to $-\pi$ (vertical lines). The experimental results however show not completely linear change of the phase and neither the local extremes correspond precisely to $+\pi$ and $-\pi$. Furthermore, the flipping of the phase is not completely vertical. All of the differences can be explained by two things: 1. The addition of the noise results in the reduction of the amplitude of the phase change and the non-vertical phase flipping (from the comparison of Fig. 3(e) and Fig. 3(f)); 2. The alignment of the measured holograms is not completely accurate due to the small drifting of the sample by SNOM measurements causing a nonlinearity of the increasing phase.

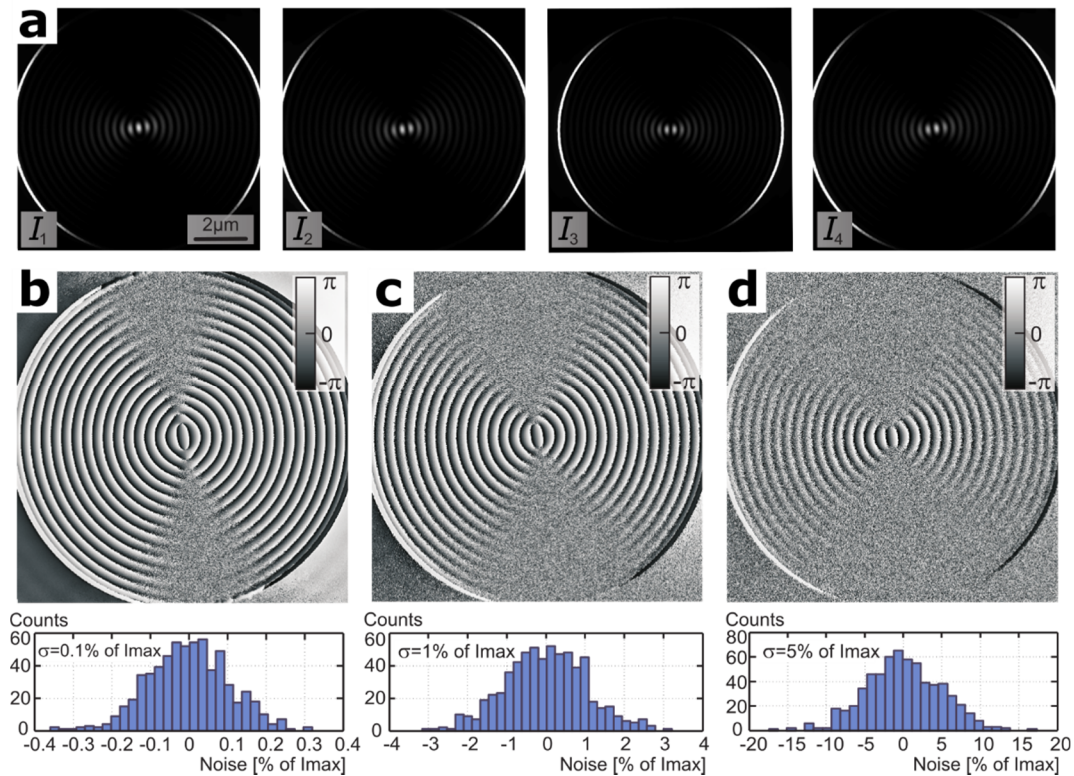


Fig. S6. a 4 measured interference patterns needed for the reconstruction of the phase image. Images b, c and d show the reconstructed phase difference image for different standard deviations of the noise affecting the measurement. The results show that the quality and the area where the phase can be reconstructed depend strongly on the noise level.

4. Testing the phase-controlled excitation of SPPs by the SLM

To demonstrate the capabilities of SLM we first applied chess-board like changes in the phase of the illumination. The active area of the SLM was divided into four quadrants in which the phase shifts of π were imposed on the light reflected from neighboring zones. In this way, the

neighboring quartiles of the circular slit are illuminated by light of an opposite phase (see Fig. S7). It is important to note, that the dark cross visible in the optical image of the illumination arises from the destructive interference of the light coming from the neighboring areas with the opposite phase, proving that phase is correctly transferred from the SLM to the sample. The resulting interference pattern is in good agreement with the simulated pattern and shows decreased intensity along the horizontal axis of mirror symmetry (in the direction of polarization) in comparison to the interference pattern without using the SLM (see Fig. S8). In our experiments - due to the dark cross appearing in the illumination spot - the chessboard-like phase mask was used as an effective tool for alignment of the illumination at the sample.

In the measured interference pattern we observed a displacement of the central interference fringe with the increasing phase shift (see Fig. S9). For the better visualization we plotted the dependence of the pattern displacement on the phase shift in Fig. 2(c) (red dots).

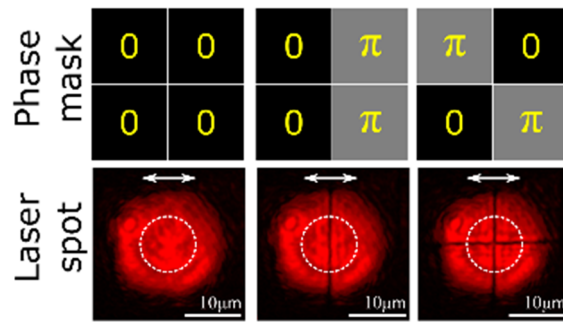


Fig. S7. The 3 different phase mask settings and the optical image of the laser spot with the highlighted direction of the laser polarization.

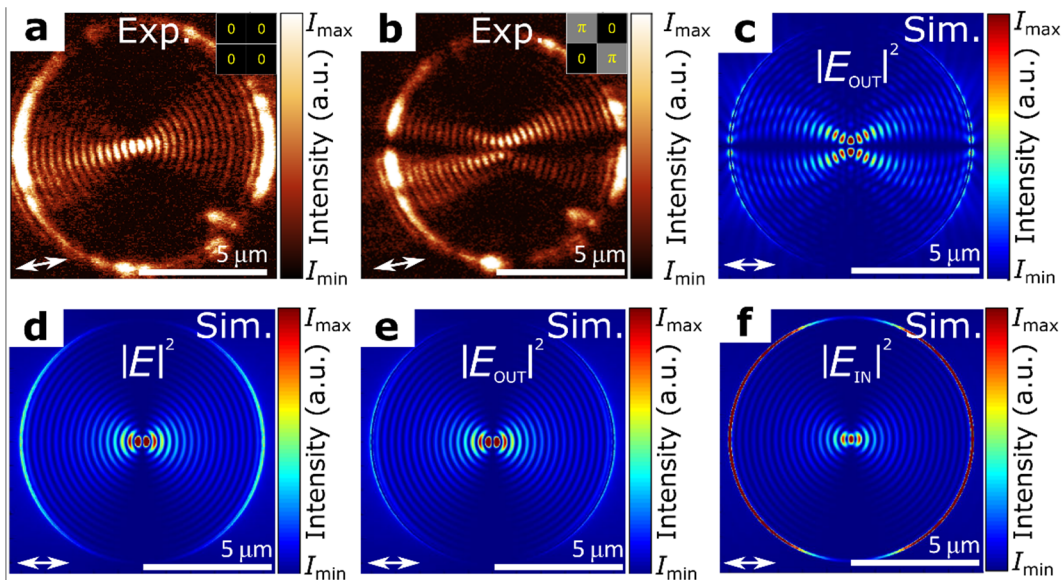


Fig. S8. **a** The measured interference pattern on the circular slit with no phase-shift and **b** with the chess-board like phase mask. **c** FDTD simulation of the interference pattern corresponding to the chess-board like illumination phase, **d** the simulated field intensity with no applied spatial phase-shift, **e** and **f** the out-of-plane and the in-plane component of the electric field, respectively.

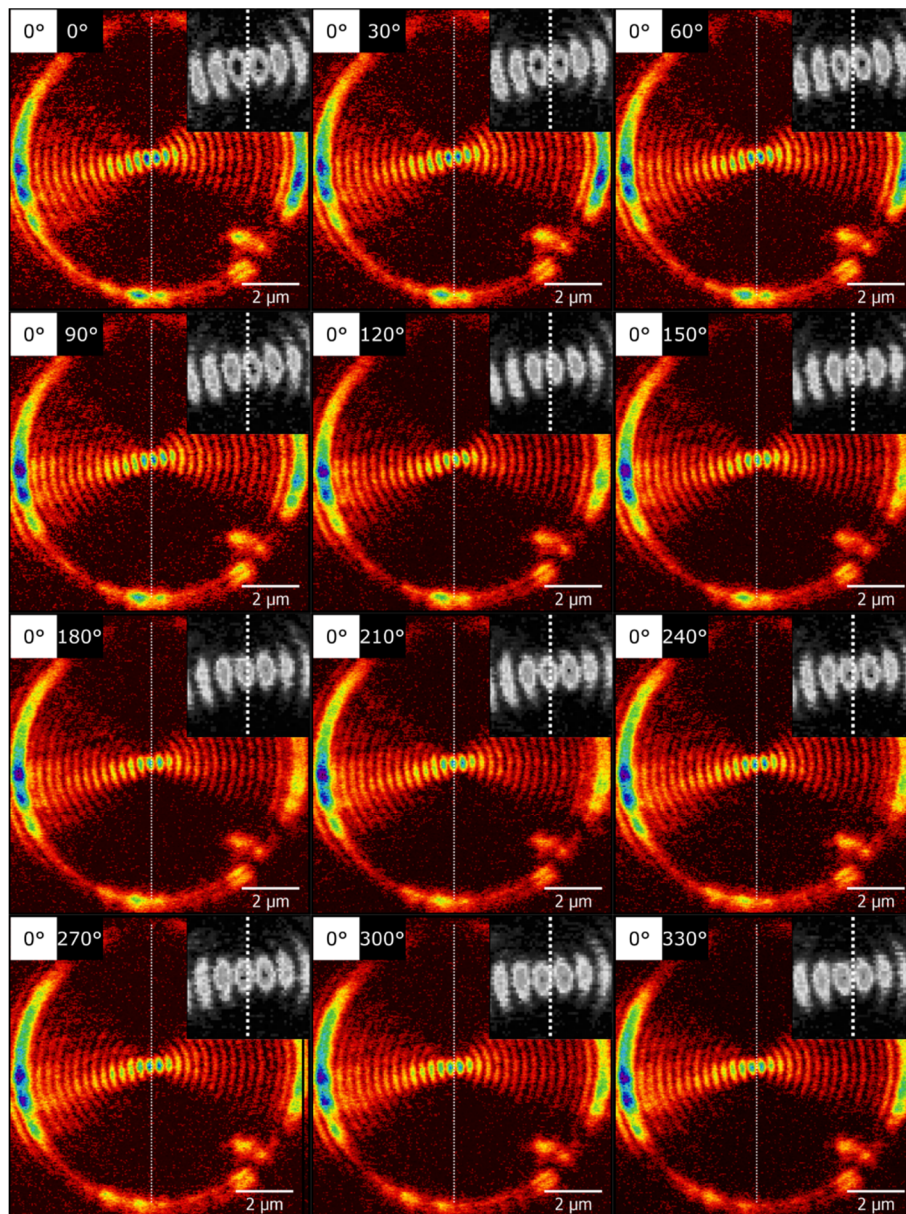


Fig. S9. The measured interference patterns for different mutual phase-shifts between the two halves of the illumination spot. The vertical dotted line shows the boundary between the two halves and the inset shows the detailed image of the centre of the interference pattern.

References

1. Chang, S.-H., Gray, S. K. & Schatz, G. C. Surface plasmon generation and light transmission by isolated nanoholes and arrays of nanoholes in thin metal films. *Opt. Express* **13**, 3150 (2005).
2. Dvořák, P. *et al.* Control and Near-Field Detection of Surface Plasmon Interference Patterns. *Nano Lett.* **13**, 2558–2563 (2013).